show relative populations as a function of the hold time and derive lifetimes as τ almost equal to 1 s, 0.5 s, and 0.2 s for the $n = 3$, $n = 4$, and $n = 5$ MI phases, respectively (Fig. 4); this is shorter than predicted, which is possibly due to secondary collisions. For $n = 1$ and $n = 2$, lifetimes of over 5 s were observed.

We expect that this method can be used to measure the number statistics as the system undergoes the phase transition. One would expect that the spectral peaks for higher occupation number become pronounced only at higher lattice depth; an indication of this can be seen already in Fig. 1. For low lattice depths, the tunneling rate is still high, but one can suddenly increase the lattice depth and freeze in populations (*19*), which can then be probed with high-resolution spectroscopy. Fluctuations in the atom number could identify the superfluid layers between the Mott shells. In addition, by applying a magnetic gradient across the lattice, tomographic slices could be selected, combining full 3D resolution with spectral resolution of the site occupancy. These techniques may address questions about local properties that have been raised in recent theoretical simulations (*20*). The addressability of individual shells could be used to create systems with only selected occupation numbers (e.g., by removing atoms in other shells). Such a preparation could be important for the implementation of quantum gates, for which homogenous filling is desirable. For atoms other than rubidium, atomic clock shifts are much larger, e.g., for sodium, larger by a factor of 30. Therefore, it should be easier to resolve the MI shells, unless the collisional lifetime of the upper state of the clock transition sets a severe limit to the pulse duration.

Note added in proof: After submission of this work, the vertical profile of an $n = 2$ MI shell was obtained by using spin-changing collisions and a magnetic resonance imaging technique (*21*).

References and Notes

1. D. Jaksch, C. Bruder, J. I. Cirac, C. W. Gardiner, P. Zoller, *Phys. Rev. Lett.* **81**, 3108 (1998).
2. G. G. Batrouni *et al.*, *Phys. Rev. Lett.* **89**, 117203 (2002).
3. B. Marco, C. Lannert, S. Vishveshwara, T. C. Wei, *Phys. Rev. A.* **71**, 063601 (2005).
4. M. Greiner, O. Mandel, T. Esslinger, T. W. Hänsch, I. Bloch, *Nature* **415**, 39 (2002).
5. I. Bloch, *Nature Phys.* **1**, 23 (2005).
6. T. Stöferle, H. Moritz, C. Schori, M. Köhl, T. Esslinger, *Phys. Rev. Lett.* **92**, 130403 (2004).
7. S. Fölling *et al.*, *Nature* **434**, 481 (2005).
8. T. Volz *et al.*, published online 8 May 2006 (http://arxiv.org/abs/cond-mat?papernum=0605184).
9. F. Gerbier, S. Fölling, A. Widera, O. Mandel, I. Bloch, *Phys. Rev. Lett.* **96**, 090401 (2006).
10. M. P. A. Fisher, P. B. Weichman, G. Grinstein, D. S. Fisher, *Phys. Rev. B* **40**, 546 (1989).
11. D. M. Harber, H. J. Lewandowski, J. M. McGuirk, E. A. Cornell, *Phys. Rev. A.* **66**, 053616 (2002).
12. K. Gibble, S. Chu, *Phys. Rev. Lett.* **70**, 1771 (1993).
13. C. Fertig, K. Gibble, *Phys. Rev. Lett.* **85**, 1622 (2000).
14. Y. Sortais *et al.*, *Phys. Scr.* **T95**, 50 (2001).
15. J. Stenger *et al.*, *Phys. Rev. Lett.* **82**, 4569 (1999).
16. E. G. M. van Kempen, S. J. J. M. F. Kokkelmans, D. J. Heinzen, B. J. Verhaar, *Phys. Rev. Lett.* **88**, 093201 (2002).
17. G. Baym, C. J. Pethick, *Phys. Rev. Lett.* **76**, 6 (1996).
18. M. W. Jack, M. Yamashita, *Phys. Rev. A* **67**, 033605 (2005).
19. M. Greiner, O. Mandel, T. W. Hänsch, I. Bloch, *Nature* **419**, 51 (2002).
20. O. Gygi, H. G. Katzgraber, M. Troyer, S. Wessel, G. G. Batrouni, *Phys. Rev. A.* **73**, 063606 (2006).
21. S. Fölling, A. Widera, T. Mueller, F. Gerbier, I. Bloch, published online 23 June 2006 (http://arxiv.org/abs/cond-mat?papernum=0606592).

22. The authors thank I. Bloch and S. Fölling for insightful discussions. This work was supported by NSF. L.G.M. also acknowledges support from Fundação de Apoio a Pesquisa do Estrado de São Paulo.

23 May 2006; accepted 7 July 2006
10.1126/science.1130365

Evidence for a Past High-Eccentricity Lunar Orbit

Ian Garrick-Bethell,* Jack Wisdom, Maria T. Zuber

The large differences between the Moon's three principal moments of inertia have been a mystery since Laplace considered them in 1799. Here we present calculations that show how past high-eccentricity orbits can account for the moment differences, represented by the low-order lunar gravity field and libration parameters. One of our solutions is that the Moon may have once been in a 3:2 resonance of orbit period to spin period, similar to Mercury's present state. The possibility of past high-eccentricity orbits suggests a rich dynamical history and may influence our understanding of the early thermal evolution of the Moon.

The Moon is generally thought to have accreted close to the Earth and migrated outwards in a synchronously locked low-eccentricity orbit. During the early part of this migration, the Moon was cooling and continually subjected to tidal and rotational stretching. The principal moments of inertia $A < B < C$ of any satellite are altered in a predictable way by deformation due to spin and tidal attraction. The moments are typically characterized by ratios that are easier to measure, namely, the libration parameters $\beta = (C - A)/B$ and $\gamma = (B - A)/C$, and the degree-2 spherical-harmonic gravity coefficients $C_{20} = (2C - B - A)/(2Mr^2)$ and $C_{22} = (B - A)/(4Mr^2)$, where M and r are the satellite mass and radius. Of these four values β, γ, and C_{20} can be taken as independent. Using the ratio $(C - A)/A$, Laplace was the first to observe that the lunar moments are not in equilibrium with the Moon's current orbital state (*1*). He did not, however, address the possibility of a "fossil bulge," or the frozen remnant of a state when the Moon was closer to the Earth. Sedgwick examined the lunar moments in 1898, as did Jeffreys in 1915 and 1937, and both authors effectively showed that β is too large for the current orbit, suggesting that the Moon may carry a fossil bulge (*2*–*5*). However, Jeffreys showed that the fossil hypothesis might be untenable because the ratio of $\gamma/\beta = 0.36$ does not match the predicted ratio of 0.75 for a circular synchronous orbit (equivalently, $C_{20}/C_{22} = 9.1$, instead of the predicted ratio of 3.33). Indeed, using data from (*6*), none of the three independent measures of moments represent a low-eccentricity synchronous-orbit hydrostatic form; $C_{20} = 2.034 \times 10^{-4}$ is 22 times too large for the current state, and $\beta = 6.315 \times 10^{-4}$ and $\gamma = 2.279 \times 10^{-4}$ are 17 and 8 times too large, respectively (*7*, *8*).

The inappropriate ratio of γ/β or C_{20}/C_{22} has led some to dismiss the fossil bulge hypothesis as noise due to random density anomalies (*9*, *10*). However, the power of the second-degree harmonic gravity field is anomalously high when compared to the power expected from back extrapolating the power of higher harmonics (*7*, *11*). This suggests that the bulge may be interpreted as a signal of some process. Degree-2 mantle convection has been proposed as a means of deforming the Moon (*12*, *13*), but the dissimilarity of all three principal moments violates the symmetry of any simple degree-2 convection model (*12*). The Moon's center-of-mass/center-of-figure offset influences the moment parameters slightly, but that problem is geophysically separate and mathematically insignificant to the degree-2 problem (*8*, *14*).

Because C_{20} is due primarily to rotational flattening, and C_{22} is due to tidal stretching, the high C_{20}/C_{22} ratio seems to imply that the Moon froze in its moments while rotating faster than synchronous. However, in such cases no constant face would be presented to the Earth for any C_{22} power to form in a unique lunar axis. This apparent dilemma can be avoided by considering that in any eccentric orbit with an orbit period to spin period ratio given by n:2, with n = 2, 3, 4, …, the passage through pericenter results in higher C_{22} stresses throughout a single elongated axis (hereafter called the pericenter axis). When the stresses experienced over one orbit period are time-averaged, the highest stresses

Department of Earth, Atmospheric and Planetary Sciences, Massachusetts Institute of Technology, 77 Massachusetts Avenue, Cambridge, MA 02139, USA.

*To whom correspondence should be addressed. E-mail: iang@mit.edu

will still appear in the pericenter axis, despite the shorter dwell time near pericenter. This is because, with respect to orbital distance, the tidal forces acting near pericenter increase faster than the decrease in time spent near pericenter.

Higher average stresses can form a C_{22} semipermanent bulge through the pericenter axis because higher stresses lead to increased strain rate. Therefore, for lunar material having both viscous and elastic properties (e.g., approximated as a Maxwell material), any higher time-averaged stresses will accumulate as higher strains, as long as the material's relaxation time is substantially longer than the period of the orbit. Because the young lunar surface must at some point cool from a liquid to a solid, it will certainly pass through a state in which the relaxation time exceeds the orbit period. This pericenter axis deformation process will also take place for a high-eccentricity synchronous orbit, where strong librational tides move the location of the C_{22} bulge over the lunar sphere, but on average the pericenter axis still attains the highest stresses.

Eventually, a semipermanent bulge that is stable on time scales of the lunar orbit must be made permanent over billions of years. The lithosphere's ability to support degree-2 spherical harmonic loads for >4 billion years is well established by theoretical calculations (*15*), and the overcompensation of large-impact basins suggests that the Moon has supported substantial lithospheric loads from an early time (*16*). The transition between the state of short and long relaxation time must also happen relatively quickly for the shape to record a particular orbital configuration. Recent isotope studies have indicated that the lunar magma ocean crystallized about 30 to 100 million years after lunar formation (*17*), and Zhong and Zuber showed that a degree-2 deformation on a 100-million-year-old lithosphere will relax only 20% of its initial deformation after 4 billion years (*15*). Therefore, a conservatively late estimate of the start of bulge freeze-in, if it took place, would be between 100 and 200 million years after lunar formation. We can obtain a rough estimate of the location of the Moon at this time by using established equations for the evolution of zero-eccentricity synchronous orbits (*18*, *19*). With a current Earth potential Love number of $k \approx 0.3$, and the quality factor for a modern oceanless Earth, $Q_{\mathrm{Earth}} = 280$ (*20*), the Moon reaches a semimajor axis of 24 r_{E} (Earth radii) by ~100 million years and 27 r_{E} by 200 million years. Therefore, over a 100-million-year time scale for fossil freeze-in, the orbit does not appreciably evolve. It will also be shown that these semimajor axis estimates are consistent with the observed libration parameters and second-degree gravity harmonics, and that our solutions permit an average fossil to develop during orbit evolution. Without better constraints on k and Q for the early Moon and Earth, and the evolution of eccentric and higher resonance orbits, no existing data rule out the development of a strong lithosphere on the relevant time scales.

To calculate eccentric orbits that may generate the time-averaged values of the three independent parameters β, γ, and C_{20}, we write the time-averaged tidal potential in each of three principal axes

$$\langle U_{t,\hat{a}}\rangle = \frac{-GMr^2}{a^3}\left(\tfrac{3}{4}X_{-3,p,q}(e) + \tfrac{1}{4}\right)$$
$$\langle U_{t,\hat{b}}\rangle = \frac{GMr^2}{a^3}\left(\tfrac{3}{4}X_{-3,p,q}(e) - \tfrac{1}{4}\right)$$
$$\langle U_{t,\hat{c}}\rangle = \frac{GMr^2}{2a^3}X_{-3,0,0}(e) \qquad (1)$$

where G is the gravitational constant; M is the Earth mass; r is the mean lunar radius (1738 km); a is the orbital semimajor axis; and $\hat{a}$, $\hat{b}$, and $\hat{c}$ refer to the principal lunar axes with respective moments $A < B < C$. The parameter $X_{l,p,q}(e)$ is the eccentricity-dependent Hansen function that arises from time averaging the orbit (*21*). A 1:1 resonance is represented by $p = 2$ and $q = 2$, whereas 3:2 and 2:1 resonances are represented by $p = 2$, $q = 3$, and $p = 2$, $q = 4$, respectively. The instantaneous potentials are recovered by replacing a with R, and $X_{l,p,q}(e)$ with $\cos(2f - 2\omega t)$, where f is the true anomaly, ω is the lunar rotational velocity, and t is the time since passage of pericenter. The rotational potentials in the principal axes can be written (*18*)

$$U_{r,\hat{a}} = U_{r,\hat{b}} = -\tfrac{1}{2}U_{r,\hat{c}} = -\tfrac{1}{6}\omega^2 r^2 \qquad (2)$$

The lunar radii due to these potentials can be expressed by $r_{\hat{a},\hat{b},\hat{c}} = -h_2\langle U_{\hat{a},\hat{b},\hat{c}}\rangle r^2/Gm$, where h_2 is the lunar secular displacement Love number, and m is the lunar mass (*22*). Without better constraints, we approximate the young Moon as a strengthless homogeneous body, for which $h_2 = 5/2$. After summing the centrifugal and tidal potentials, we may obtain $r_{\hat{a},\hat{b},\hat{c}}$ for any orbit. Given the moment relations $A \propto r_{\hat{b}}{}^2 + r_{\hat{c}}{}^2$, $B \propto r_{\hat{a}}{}^2 + r_{\hat{c}}{}^2$, $C \propto r_{\hat{a}}{}^2 + r_{\hat{b}}{}^2$, the gravity harmonic $C_{20} = [r_{\hat{c}} - \tfrac{1}{2}(r_{\hat{a}} + r_{\hat{b}})]/5r^2$ (*23*), and the definitions of β and γ given previously, we obtain for a 3:2 resonance

$$C_{20} = \frac{Mr^3}{ma^3}\left(-\tfrac{1}{2}X_{-3,0,0}(e) - \tfrac{11}{8}\right)$$
$$\beta = \tfrac{5}{2}\frac{Mr^3}{ma^3}\left(\tfrac{1}{2}X_{-3,0,0}(e) + \tfrac{3}{4}X_{-3,2,3}(e) + \tfrac{11}{8}\right)$$
$$\gamma = \tfrac{15}{4}\frac{Mr^3}{ma^3}X_{-3,2,3}(e) \qquad (3)$$

Similarly, for synchronous rotation, we obtain

$$C_{20} = \frac{Mr^3}{ma^3}\left(-\tfrac{1}{2}X_{-3,0,0}(e) - \tfrac{3}{4}\right)$$
$$\beta = \tfrac{5}{2}\frac{Mr^3}{ma^3}\left(\tfrac{1}{2}X_{-3,0,0}(e) + \tfrac{3}{4}X_{-3,2,2}(e) + \tfrac{3}{4}\right)$$
$$\gamma = \tfrac{15}{4}\frac{Mr^3}{ma^3}X_{-3,2,2}(e) \qquad (4)$$

These equations approximate the tidal and rotational effects for nonchanging orbits of arbitrary eccentricity.

We searched the a-e space of Eqs. 3 and 4 to find minimum-error solutions to the observed values of β, γ, and C_{20}. For synchronous rotation we find one solution at $a = 22.9$ r_{E}, $e = 0.49$; and for 3:2 resonance we find two solutions at $a = 24.8$ r_{E}, $e = 0.17$, and, $a = 26.7$ r_{E}, $e = 0.61$. One means of visualizing how closely these solutions match the observed values is to plot the a-e solutions for each parameter in a-e space (Figs. 1 and 2). For a Moon frozen instantaneously into the average potentials of a given orbit, the values of the solution curves of β, γ, and C_{20} will intersect at a single point. The insets in Figs. 1 and 2 show that the calculated solutions intersect quite near each other. That is, the Moon's observed moments closely satisfy a specific set of orbital constraints on the ratio of β, γ, and C_{20}. To see this effect more clearly, imagine, for example, if the value of the observed C_{20} was smaller by 20%, i.e., closer to producing the value of 3.33 for the ratio C_{20}/C_{22}. In this case the curves would no longer intersect so closely, and the results would be more inconclusive (Fig. 1). Currently, altering either β or C_{20} by about 2%, or γ by 8%, will bring the lines into a perfect intersection, a much smaller difference than the discrepancies discussed in the first paragraph.

The Moon may have relaxed somewhat since freeze-in, but because β, γ, and C_{20} would have relaxed equally, the observed solution would merely be a horizontal displacement in semimajor axis from an earlier three-way intersection. For example, Fig. 2 shows a 3:2 resonance solution for the values of 2β, 2γ, and $2C_{20}$ ($a = 19.6$ r_{E}, $e = 0.17$), i.e., if the current values are relaxed by 50%. More generally, the Moon need not have frozen instantaneously to produce the moments we observe. The average of the values of β, γ, and C_{20} for any two solutions in a-e space produces a valid third solution, so that an evolving orbit may produce not a single true fossil, but a combination (*14*, *24*). For example, in the case of 3:2 resonance, if the Moon started freezing its figure at $a = 23$ r_{E}, $e = 0.2$, the observed values of β, γ, and C_{20} would be higher by a factor of 1.28, 1.43, and 1.27, respectively. Later, if the Moon evolved to an orbit at $a = 27$ r_{E}, $e = 0.12$, and completed its freeze-in there, we would have at that location 0.73β, 0.57γ, and 0.78C_{20} (Fig. 2). These final and initial parameters average very close to the observed values, but they are not uniformly lower by a single factor, as would be expected for parameters changed by relaxation alone. Therefore, the requirement that the Moon changed rapidly from a state of short relaxation time to long relaxation time is not a stringent one. Combining relaxation and multiple averages over an evolving orbit, a rich history is permitted by the single observed solution.

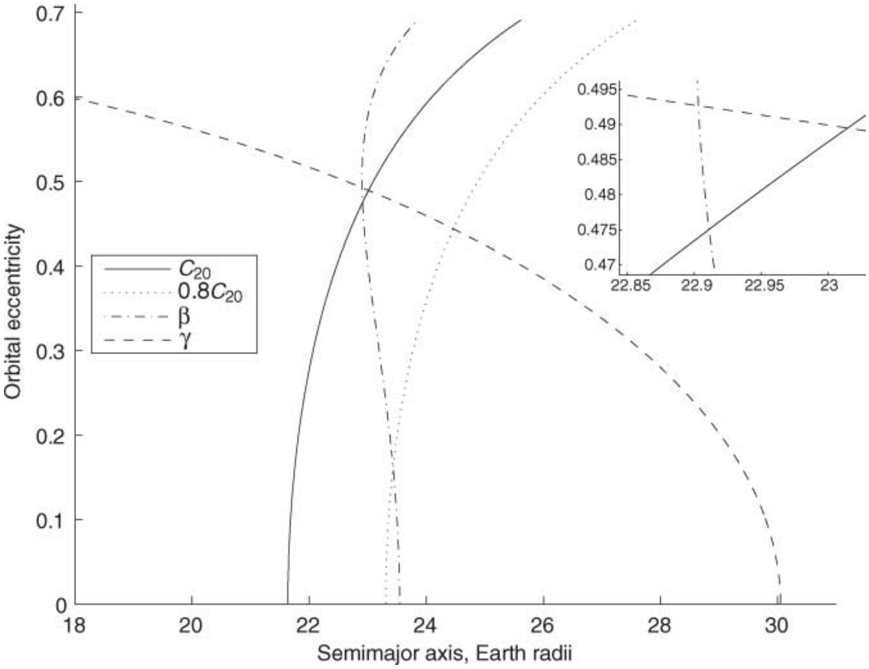

Fig. 1. Synchronous orbit solutions in a and e that give the observed values of β, γ, and C_{20} (Eq. 4). Valid a-e solutions to a hypothetical 0.8C_{20} are plotted to show the uniqueness of the observed parameters β, γ, and C_{20}. (**Inset**) Close-up of the intersection.

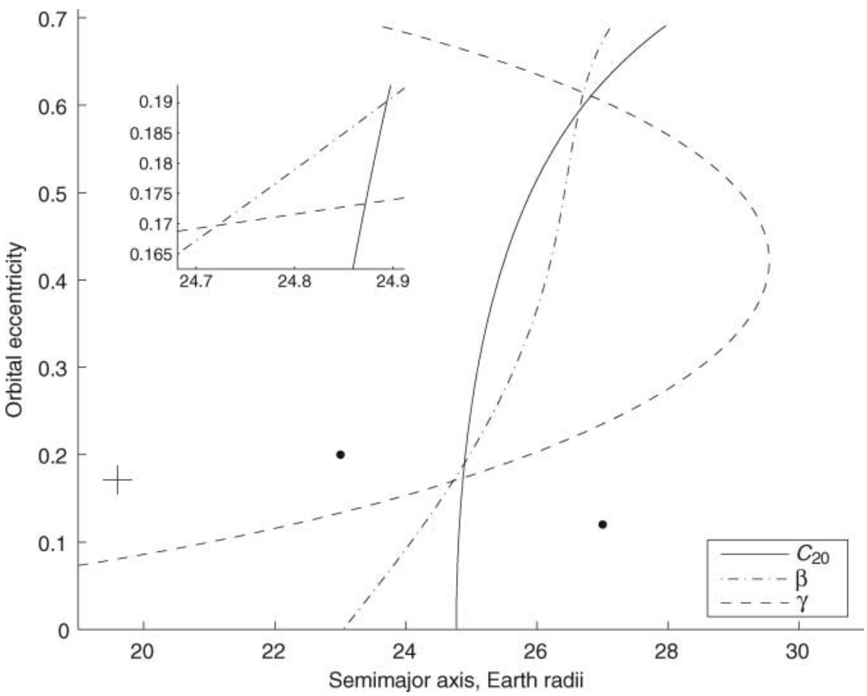

Fig. 2. 3:2 resonance solutions in a and e that give the observed values of β, γ, and C_{20} (Eq. 3). The cross at r_E = 19.6, e = 0.17, shows an orbit solution if the current values of β, γ, and C_{20} are from a fossil bulge that has relaxed by 50%. The two dots show solutions that average to the observed values of β, γ, and C_{20}. (**Inset**) Close-up of the bottom intersection.

We also find solutions for 2:1 resonance at a = 28.6 r_E, e = 0.39, and a = 29.0 r_E, e = 0.52. No one solution for any orbital state is better constrained over the others by the values β, γ, and C_{20}. However, we may interpret which state is more likely in the context of what we presently know about the orbital evolution of the Moon and Mercury. Past high-eccentricity orbits for the Moon have been considered possible for some time (*22*, *25*), and it is interesting to note that the Moon's eccentricity is the highest of all solar system satellites with radius > 200 km. In general, torques on a satellite from tides raised on the primary body will increase eccentricity, whereas energy dissipation in the satellite due to tides raised by the primary body will decrease eccentricity. Peale gives an expression for the energy dissipation rate in a low-eccentricity synchronous orbit (*26*), but there are no readily available expressions for orbits with higher-order resonances. Deriving new expressions and interpreting plausible orbital histories are not possible in the limited space here, but we note that for any combination of e, k, and Q of the Earth and Moon, there will be a critical initial eccentricity above which eccentricity may start to increase. Touma and Wisdom have also studied in detail the process by which a synchronously rotating Moon can be excited into high eccentricity (e = 0.5) at a = 4.6 r_E, in a resonance known as the evection (*27*). Numerical models of lunar accretion give initial eccentricities that range from 0 to 0.14 (*28*).

It has long been considered that the Moon may have passed through resonances higher than synchronous (*22*, *29*, *30*), and it is believed that Mercury passed through resonances higher than 3:2 (*29*, *31*). Among the solar system satellites, the Moon has one of the highest capture probabilities into 3:2 resonance (*30*). Formation by giant impact would leave the Moon to form near 4 r_E (*28*), where synchronous orbital periods would be greater than 10 hours. The initial spin period of the Moon may be as low as 1.8 hours before reaching rotational instability (*30*), leaving open the possibility of sufficient angular momentum to permit greater than synchronous resonances.

The probability of capture into resonance generally decreases with the order of the resonance (*29*), so capture in the 3:2 resonance is more likely than the 2:1 resonance. As for the high-e solutions for synchronous rotation and 3:2 resonance, these orbits dissipate energy faster and would change orbital parameters faster than their low-e counterpart. The low-e 3:2 solution may therefore have the slowest evolving orbit, which may be more compatible with freeze-in. The k and Q values for the very young Moon and Earth, possible formation of the Moon nearer the evection point, and variations in initial eccentricity all affect the probability of achieving a 3:2 resonance. In any case, the Moon must have eventually escaped any past 3:2 state, possibly through eccentricity damping. None of the above processes in early lunar evolution are well explored.

References and Notes

1. P.-S. Laplace, *Traité de Mécanique Céleste* (Paris Duprat, Bachlier 1798-1827), vol. 2, book 5, chap. 2.
2. W. F. Sedgwick, *Messenger Math.* **27**, 171 (1898).
3. H. Jeffreys, *Mem. R. Astron. Soc.* **60**, 187 (1915).
4. H. Jeffreys, *Mon. Not. R. Astron. Soc. Geophys. Suppl.* **4**, 1 (1937).
5. H. Jeffreys, *The Earth* (Cambridge Univ. Press, Cambridge, 1970).
6. A. S. Konopliv *et al.*, *Science* **281**, 1476 (1998).
7. J. G. Williams, D. H. Boggs, C. F. Yoder, J. T. Ratcliff, J. O. Dickey, *J. Geophys. Res.* **106**, 27933 (2001).
8. Z. Kopal, *Proc. R. Soc. London Ser. A* **296**, 254 (1967).
9. P. Goldreich, A. Toomre, *J. Geophys. Res.* **74**, 2555 (1969).
10. M. Lefftz, H. Legros, *Phys. Earth Planet. Inter.* **76**, 317 (1993).
11. K. Lambeck, S. Pullan, *Phys. Earth Planet. Inter.* **22**, 29 (1980).
12. S. K. Runcorn, *Nature* **195**, 1150 (1962).
13. P. Cassen, R. E. Young, G. Schubert, *Geophys. Res. Lett.* **5**, 294 (1978).
14. D. J. Stevenson, *Proc. Lunar Planet. Sci. Conf.* XXXII, abstract 1175 (2001).
15. S. Zhong, M. T. Zuber, *J. Geophys. Res.* **105**, 4153 (2000).
16. G. A. Neumann, M. T. Zuber, D. E. Smith, F. G. Lemoine, *J. Geophys. Res.* **101**, 16841 (1996).
17. T. Kleine, H. Palme, K. Mezger, A. N. Halliday, *Science* **310**, 1671 (2005).
18. C. D. Murray, S. F. Dermott, *Solar System Dynamics* (Cambridge Univ. Press, Cambridge, 1999).
19. J. Touma, J. Wisdom, *Astron. J.* **108**, 1943 (1994).
20. R. D. Ray, R. J. Eanes, F. G. Lemoine, *Geophys. J. Int.* **144**, 471 (2001).
21. The Hansen functions, $X_{l,p,q}(e)$, satisfy $\left(\frac{R}{a}\right)^l \cos(pf) = \sum_q X_{l,p,q}(e)\cos(q\tilde{M})$ (*32*), where f is the true anomaly and $\tilde{M}$ is the mean anomaly. For our purposes, $l = -3$. The Hansen functions are also called Hansen coefficients, and the expansions in e to fourth order can be found in table 3.2 of (*33*), albeit with a different subscript convention.
22. S. J. Peale, P. Cassen, *Icarus* **36**, 245 (1978).
23. C. F. Yoder, in *Global Earth Physics*, T. J. Ahrens, Ed. (American Geophysical Union, Washington, DC, 1995), p. 1.
24. The simple average of two different sets of parameters β, γ, and C_{20} may take place during the transition from the state of low relaxation time to the state of long relaxation time. During this time, the Moon is plastic enough to accommodate changes in form, yet stiff enough to retain some signature of its state when freeze-in started. Indeed, the Moon is necessarily a sum of different orbits, however close or far apart, if the fossil bulge hypothesis is valid.
25. P. Goldreich, *Mon. Not. R. Astron. Soc.* **126**, 257 (1963).
26. S. J. Peale, *Celest. Mech. Dyn. Astron.* **87**, 129 (2003).
27. J. Touma, J. Wisdom, *Astron. J.* **115**, 1653 (1998).
28. E. Kokubo, S. Ida, J. Makino, *Icarus* **148**, 419 (2000).
29. P. Goldreich, S. J. Peale, *Astron. J.* **71**, 425 (1966).
30. S. J. Peale, in *Satellites*, J. A. Burns, Ed. (Univ. of Arizona Press, Tucson, 1978), p. 87.
31. Mercury's unnormalized coefficients $C_{20} = 6 \times 10^{-5} \pm 2.0$ and $C_{22} = 1 \times 10^{-5} \pm 0.5$ (*34*) are not reproduced by any orbit-spin resonance at Mercury's current semimajor axis.
32. H. C. Plummer, *An Introductory Treatise on Dynamical Astronomy* (Dover, New York, 1960).
33. W. M. Kaula, *Theory of Satellite Geodesy* (Dover, New York, 1966).
34. J. D. Anderson, G. Colombo, P. B. Esposito, E. L. Lau, G. B. Trager, *Icarus* **71**, 337 (1987).

35. We are grateful to B. Hager and B. Weiss for helpful comments. This work was supported by NASA Planetary Geology and Geophysics Program grants (to M.T.Z. and J.W.).

3 April 2006; accepted 8 June 2006
10.1126/science.1128237

Smoke and Pollution Aerosol Effect on Cloud Cover

Yoram J. Kaufman[1] and Ilan Koren[2]*

Pollution and smoke aerosols can increase or decrease the cloud cover. This duality in the effects of aerosols forms one of the largest uncertainties in climate research. Using solar measurements from Aerosol Robotic Network sites around the globe, we show an increase in cloud cover with an increase in the aerosol column concentration and an inverse dependence on the aerosol absorption of sunlight. The emerging rule appears to be independent of geographical location or aerosol type, thus increasing our confidence in the understanding of these aerosol effects on the clouds and climate. Preliminary estimates suggest an increase of 5% in cloud cover.

Aerosol particles originating from urban and industrial pollution or smoke from fires have been shown to affect cloud microphysics, cloud reflection of sunlight to space, and the onset of precipitation (*1*, *2*). Delays in the onset of precipitation can increase the cloud lifetime and thereby increase cloud cover (*3*, *4*). Research on the aerosol effect on clouds and precipitation has been conducted for half a century (*5*). Although we well understand the aerosol effect on cloud droplet size and reflectance, its impacts on cloud dynamics and regional circulation are highly uncertain (*3*, *5–9*) because of limited observational information and complex processes that are hard to simulate in atmospheric models (*10*, *11*). Indeed, global model estimates of the radiative forcing due to the aerosol effect on clouds range from 0 to –5 W/m^2. The reduction of this uncertainty is a major challenge in improving climate models.

[1]NASA/Goddard Space Flight Center, 613.2, Greenbelt, MD 20771, USA. [2]Department of Environmental Sciences and Energy Research, Weizmann Institute, Rehovot 76100, Israel.

*To whom correspondence should be addressed. E-mail: ilan.koren@weizmann.ac.il

Satellite measurements show strong systematic correlations among aerosol loading, cloud cover (*12*), and cloud height over the Atlantic Ocean (*13*) and Europe (*14*), making the model estimates of aerosol forcing even more uncertain. However, heavy smoke over the Amazon forest (*15*) and pollution over China (*16*) decrease the cloud cover by heating the atmosphere and cooling the surface (*17*) and may balance some of this large negative forcing. Global climate models also show a reduction in cloud cover due to aerosol absorption (τ_{abs}) outside (*18*) and inside the clouds (*19*). In addition, the aerosol effect on slowing down the hydrological cycle by cooling parts of the oceans (*1*) may further reduce cloud formation and the aerosol forcing. Understanding these aerosol effects on clouds and climate requires concentrated efforts of measurement and modeling of the effects.

There are several complications to devising a strategy to measure the aerosol effect on clouds. Although clouds are strongly affected by varying concentrations of aerosol particles, they are driven by atmospheric moisture and stability. Local variations in atmospheric moisture can affect both cloud formation and aerosol humidification, resulting in apparent correlations between aerosol column concentration and cloud cover (*12*, *13*, *20*). In addition, chemical processing of sulfates in clouds can affect the aerosol mass concentration for aerosol dominated by sulfates.

We attempt to address these issues by introducing an additional measurement dimension. We stratified the measurements of the aerosol effect on cloud cover as a function of τ_{abs} of sunlight, thus merging in one experiment both the aerosol enhancement and inhibition of cloud cover. Because the concentration of the absorbing component of aerosols is a function of the aerosol chemical composition, rather than aerosol humidification in the vicinity of clouds, this concentration can serve as a signature for the aerosol effect on clouds. A robust correlation of cloud cover with aerosol column concentration and τ_{abs} in different locations around the world can strengthen the quantification of the aerosol effect on cloud cover, though a direct cause-and-effect relationship will await detailed model simulations.

Table 1. Slopes and intercepts of $\Delta f_{ci}/\Delta\ln\tau$ versus τ_{abs} (Fig. 3A) for the complete data set (All data), continental data dominated by air pollution aerosol, coastal stations, and stations dominated by biomass burning. Results are given for (i) absolute change of the independent cloud fraction Δf_{ci} versus the optical depth $\Delta f_{ci}/\Delta\ln\tau$ and for (ii) partial change $\delta f_{ci}/\delta\ln\tau$ from a multiple regression of Δf_{ci} with $\ln\tau$ and total precipitable water vapor.

	Slope versus τ_{abs}		Intercept for $\tau_{abs} = 0$	
	$\Delta f_{ci}/\Delta\ln\tau$	$\delta f_{ci}/\delta\ln\tau$	$\Delta f_{ci}/\Delta\ln\tau$	$\delta f_{ci}/\delta\ln\tau$
All data	–3.5	–2.6	0.17	0.13
Continental	–3.2	–2.6	0.16	0.13
Coastal	–3.4	–1.9	0.17	0.11
Biomass burning	–4.0	–3.5	0.18	0.14